Growth Mechanism of Dendritic Hematite via Hydrolysis of Ferricyanide

Alice E. Green, Chang-Yang Chiang, Heather F. Greer, Ashleigh Waller, Aron Ruszin, James Webster, Ziyin Niu, Katherine Self and Wuzong Zhou*

EaStChem, School of Chemistry, University of St Andrews, St Andrews, KY16 9ST, United Kingdom.

ABSTRACT: The detailed process of the hydrolysis of ferricyanide into dendritic α-Fe_2O_3 (hematite) crystals with snowflake-like, feather-like and leaf-like morphologies has been investigated. $[Fe(CN)_6]^{3-}$ anions were found to polymerize into large, disordered soft matter aggregates at an early stage. The nucleation of hematite crystals took place near the surface of these aggregates via further hydrolysis. After the crystals grew to a certain size, branches started to appear. When the concentration of ferricyanide was low (*i.e.* 2 mM to 3.8 mM), growth was preferentially along the six equivalent <11$\bar{2}$0> directions, resulting in a flat snowflake-like shape, while high concentrations (*i.e.* 9 mM to 500 mM) of ferricyanide led to the growth of selective directions along the <10$\bar{1}$1> zone axes, forming a feather-like or leaf-like morphology. Highly selective adsorption and surface hydrolysis of $[Fe(CN)_6]^{3-}$ anions on α-Fe_2O_3 crystals was found to be a crucial process in the formation of these novel morphologies. It was found that the polymerisation of ferricyanide led to a reduction of pH value and that the formation of Fe_2O_3 increased pH value. The pH value of the solution at the point when the branches start to grow can significantly affect the distribution of Lewis acidic sites on different surfaces and, therefore, change the growth direction. The newly established mechanism is complementary to the classical theories of crystal growth.

INTRODUCTION

Control over crystal growth orientation, exposure of selected crystal facets, and formation of novel crystal morphologies are hot topics in crystal engineering and in materials science, since the morphology and size of crystals often have a significant effect on their physio-chemical properties.[1]

Two classical theories are normally used to elucidate morphology formation of free crystals. One is Bravais-Friedel-Donnay-Harker (BFDH) law,[2-4] where the appearance of facets of a crystal is attributed to slow growth rates along these directions, since the faces on the fast growing directions would grow out. Another is a thermodynamic approach described by Curie-Wulff theorem:[5,6] the equilibrium shape of a crystal is the shape that minimizes its surface free energy. Consequently, crystals often have highly symmetric polyhedral shapes.

However, a real crystal growth system could be much more complicated. To understand the mechanism of crystal growth, we must not only take the energy of the target crystals into account, but also consider their environment. For example, a perfect polyhedral morphology is not always a sign of a single crystal. At an early stage of crystal growth, if the interactions between precursor molecules/ions or between nanocrystallites are strong, they can aggregate into large disordered particles. The environment for the growth of free crystals is therefore disturbed. The most active sites for crystallization are at the particle surfaces, where crystallization of amorphous precursors or re-crystallization of nanocrystallites would lead to the formation of a single crystalline polyhedral shell with a disordered core. The crystallization would then extend from the surface to the core, producing true single crystals. This is the so-called reversed crystal growth mechanism, which has been observed from several crystal growth systems.[7-10]

To synthesise low dimensional materials, *e.g.* nanowires, some special conditions are normally applied to partially block crystal growth directions. For example, during the catalytic growth of Si nanowires on Au nanoparticles, the growth site is the interface between Si and Au. The diameter of the Si nanowires is, therefore, restricted by the size of the Au particles.[11,12] Growth of metal oxides in pores of mesoporous silica can result in nanowires or porous single crystals.[13,14] In this case, the crystal growth is confined by the pore size. One dimensional growth to form nanorods or nanowires can also be achieved by surface protection with ligands,[15,16] or by using porous templates such as anodic aluminum oxide.[17] Very long C_{60}/trimethylbenzene composite nanowires can grow via the evaporation of solvent from a thin layer of C_{60}/trimethylbenzene solution, where the diameter of the nanowires is controlled by the thickness of the solution layer.[18,19] In the above cases, the external factors, that restrict crystal growth, are obvious (*i.e.* mostly templating).

On the other hand, the growth of free crystals without templates or surface adsorbed ligands does not always lead to a polyhedral morphology. For example, the formation of snowflakes (a typical example of ice crystals) cannot be explained using BFDH law or Curie-Wulff theorem. Hematite (α-Fe_2O_3) can also form a snowflake-like shape via the hydrolysis of $[Fe(CN)_6]^{3-}$ anions.[20] In our recent work, we confirmed that the formation of snowflake hematite relies on highly selective crystal growth directions along the six equivalent <11$\bar{2}$0> axes of the rhombohedral structure with the unit cell parameters of a = 5.0356 and c = 13.7489 Å, space group R$\bar{3}$c (JCPDS card no. 33-0664). We further proposed that an interaction between Lewis acidic sites on the {11$\bar{2}$0} surfaces of hematite crystals and $[Fe(CN)_6]^{3-}$ anions, followed by surface hydrolysis is the key process of the crystal growth.[21] However, the detailed mechanism had not been investigated, including nucleation, primary crystal growth, branch growth and pH changes with concentration of ferricyanide and reaction time, *etc.*

α-Fe_2O_3 is the most stable phase of the four polymorphs of Fe_2O_3.[22] This compound is particularly interesting due to its wide range of properties and therefore applications. Not only is it inexpensive, environmentally friendly and resistant to corrosion, this material is useful for its antiferromagnetic and n-type semiconducting properties (Eg = 2.1 eV).[23-25] Importantly, the size and morphology of the crystals have been found to significantly change the physico-chemical properties of Fe_2O_3.[26] Snowflake-like dendritic hematite crystals have nanoscale local crystal dimensions and are dominated by the {0001} exposed surfaces. Previously, magnetic studies on dendrites, single and double-layered snowflakes, showed morphology dependent properties through variations in the coercivity values.[27] Additionally, dendritic Fe_2O_3 outperformed Fe_2O_3 nanoparticles in the degradation of methylene blue which could be further improved by grafting size-tuned Pd or Ag nanoparticles with a 12% loading on dendritic Fe_2O_3.[28] Facet controlled studies of Fe_2O_3 confirmed that crystals with predominately exposed $\{10\bar{1}1\}$ facets have a much higher photocatalytic performance than those with mostly {0001} facets exposed. This structure-activity correlation was found to be closely related to the density of exposed iron ions on the facets.[29]

Herein, we report our investigation of the step-by-step crystal growth of hematite via hydrolysis of ferricyanide anions. It has been observed that $[Fe(CN)_6]^{3-}$ anions do not undergo hydrolysis into individual hydroxide ions, followed by direct dehydration into Fe_2O_3.[21] Instead, partial hydrolysis of these anions leads to polymerization into large disordered aggregates. Such partial hydrolysis reduces the pH value of the solution to acidic conditions, while the formation of Fe_2O_3 crystals would increase the pH value to basic conditions. Shifting the start point of branch growth from basic to acidic conditions can completely change the growth orientation, leading to a morphology change from snowflake-like to feather-like or leaf-like shapes. The newly established mechanism driven by surface acidity may shed light on the elucidation of many other novel crystal morphologies.

EXPERIMENTAL SECTION

Sample preparation. Potassium hexacyanoferrate, $K_3Fe(CN)_6$ (98%, Alfa Aesar), was dissolved in 20 mL de-ionised water with more than 10 different concentrations ranging from 0.1 to 500 mM, sealed in a 30 mL autoclave and maintained at 170 ºC or 180 ºC for a range of growth times. More than 120 samples were synthesized. The synthetic conditions for some of the samples are listed in Table S1 in Supporting Information (SI). The red precipitates, designated sample (x, y) with x = concentration of ferricyanide and y = reaction time, were collected by centrifugation, washed with distilled water and ethanol, and then dried at 60 ºC for 4 h.

Sample characterization. Characterization of the samples was chiefly performed using scanning electron microscopy (SEM), transmission electron microscopy (TEM) and powder X-ray diffraction (XRD). SEM images were recorded on a JEOL JSM-6700F field-emission gun microscope, operated between 1 to 5 kV in gentle mode. To avoid beam charging, the samples were coated with a thin gold layer using a Quorum 150R ES coating system prior to insertion into the microscopic column. TEM images, high resolution TEM (HRTEM) images and selected area electron diffraction (SAED) patterns were obtained on a JEOL JEM-2011 electron microscope operated at an accelerating voltage of 200 kV, using a Gatan 794 CCD camera. Chemical compositions of the produced particles were examined using energy dispersive X-ray microanalysis (EDX) using an Oxford Instruments Link ISIS SEMI-STEM system on the JEOL JEM-2011 and Oxford Instruments INCA ENERGY system on a JEOL JSM-5600 SEM. For TEM sample preparation, the α-Fe_2O_3 sample powders were lightly ground using a pestle and mortar and suspended in acetone. One drop of the suspension was deposited onto a 3 mm sized copper grid with a thin holey carbon support film coating. The solvent was allowed to evaporate then the grid was placed in the specimen holder. XRD patterns of the samples were collected using a PANalytical Empyrean diffractometer, with CuKα radiation (λ = 1.5418 Å) operating in reflection mode. Samples were dispersed on a 0-background Si substrate. HighScore Plus software was used to analyse the resulting powder XRD patterns. pH measurements were conducted using a Fisher Scientific accumet AP6 portable pH/mV/temperature meter.

RESULTS AND DISCUSSION

SEM examination of the produced powder samples from different concentrations of ferricyanide revealed that, when the concentration was 3.8 mM or lower, the morphology of the hematite crystals was snowflake-like, while concentrations of 9 mM or higher resulted in feather-like or leaf-like morphologies (Figure 1). Variation of temperature from 170 ºC to 180 ºC had an insignificant effect on the crystal growth. In the following sections, the formation mechanisms of these morphologies will be discussed in detail based on experimental results from some typical samples.

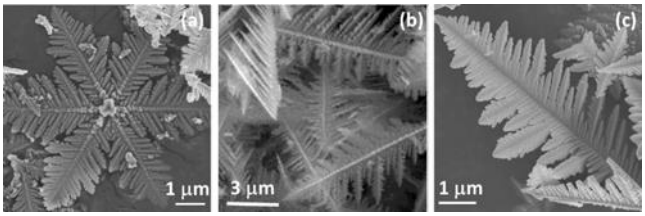

Figure 1. SEM image of hematite crystals, (a) snowflake-like in sample (3.8 mM, 2 h), (b) feather-like in sample (10 mM, 48 h), (c) leaf-like in sample (500 mM, 90 min).

Snowflake-like hematite. The present work confirms that a low concentration of potassium hexacyanoferrate, $K_3Fe(CN)_6$, leads to snowflake-like hematite crystals. In the synthesis with 2 mM $K_3Fe(CN)_6$, very little precipitate could be collected for further characterization after a short reaction of 1 h.

The early stage precipitate (2 mM, 2 h) contains mainly irregular particles as shown in Figure 2a. Although the XRD pattern showed reasonably strong diffraction peaks corresponding to hematite (see Figure S1a in SI), the majority of particles were amorphous. A typical HRTEM image is shown in Figure 2b. The corresponding SAED pattern shows no sharp diffraction spots. The EDX spectrum shows the co-existence of K, Fe, C, N, and O (see Figure S2a in SI). These results strongly suggest that the disordered aggregates are polymerized ferricyanide anions with K^+ to balance the charges.

It has been often mentioned in previous reports [30] that the formation of hematite crystals via hydrolysis of $[Fe(CN)_6]^{3-}$ is due to the reaction of

$$[Fe(CN)_6]^{3-} \rightarrow FeOOH/Fe(OH)_3 \rightarrow \alpha\text{-}Fe_2O_3 \qquad (1)$$

However, this expression of the reactions does not determine any details of the nucleation, primary crystal growth and formation of branches. In fact, the dissociation of $[Fe(CN)_6]^{3-}$ in water is extremely low with the dissociation constant, $K_d = 1.0 \times 10^{-42}$. Consequently, in the present work, before individual $[Fe(CN)_6]^{3-}$ could be completely hydrolyzed, it was likely they underwent partial hydrolysis and polymerized into dimers.

$$[Fe(CN)_6]^{3-} + H_2O \rightarrow [Fe(OH)(CN)_5]^{3-} + HCN \quad (2)$$

$$[Fe(CN)_6]^{3-} + [Fe(OH)(CN)_5]^{3-} \rightarrow [Fe(CN)_5]^{2-}\text{–O–}[Fe(CN)_5]^{2-} + HCN \quad (3)$$

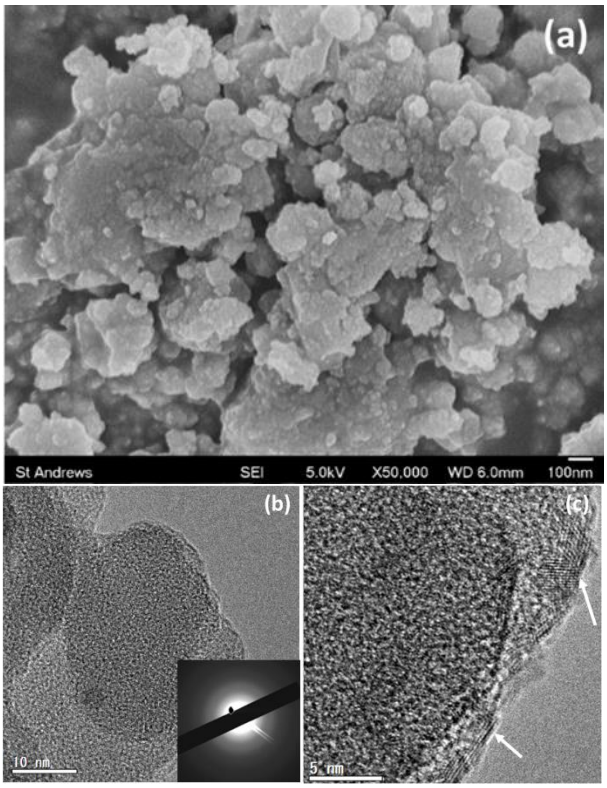

Figure 2. (a) SEM image and (b,c) HRTEM images of sample (2 mM, 2 h). The inset of (b) is the corresponding SAED pattern. The arrows in (c) indicate nanocrystallites.

followed by

$$HCN \xrightarrow{k\alpha} H+ + CN^- \quad (4)$$

Then the dimers were further polymerized into trimers, $[Fe(CN)_5]^{2-}$–O–$[Fe(CN)_4]^{-}$–O–$[Fe(CN)_5]^{2-}$, and larger polymer anions, $[Fe(CN)_5]^{2-}$–{–O–$[Fe(CN)_4]^{-}$}$_n$–O–$[Fe(CN)_5]^{2-}$. Such polymerization reduced the concentration of the precursor anions and suppressed the commonly believed process of nucleation of Fe_2O_3 in the solution. Instead, the nucleation of hematite crystals took place near the surface of polymer particles as shown in Figure 2c, where some nanocrystals, 1 to 2 nm in size, are visible. The reason for the preferential nucleation near the surface is that participation of water molecules from the solution is essential for the nucleation.

The embedded crystals grew larger and the proportion of polymer reduced gradually over time. Figure 3a shows a crystal with a diameter of about 25 nm. There is a smaller crystallite overlapping with the crystal indicated by the arrow. From its high transparency and uniform image contrast, it can be believed that the morphology of this crystallite is a thin plate. The second phenomenon observed here is that, when the crystals grew larger, certain facets became more and more apparent. The crystal size could be as large as 100 nm in diameter without the development of branches occurring (Figure 3b). These relatively large crystallites are also indicated by the diffraction peaks in the XRD pattern (see Figure S1a in SI). At this point, the large crystallites were no longer embedded in polymer and only had a very thin polymer layer coating their surfaces. Further crystal growth relied on the migration of the precursor anions to the crystal surface. Analysis of the HRTEM images confirms the hematite crystal structure. EDX results show only Fe and O without C, N and K (see Figure S2b in SI).

When the reaction time was beyond 2 h, branches rapidly developed from the central crystal. Figure 3c is a SEM image of hematite crystals with a snowflake-like morphology from sample (2 mM, 160 min). The faces of these flat particles are terminated with the {0001} planes of the rhombohedral structure. Figure 3d shows a HRTEM image of part of a primary branch with some secondary branches just starting to grow out. Analysis of this image confirms that the growth directions are <11$\bar{2}$0>, which is the same as that of the previously reported snowflake-like hematite, synthesized with a relatively higher concentration of ferricyanide anions (3.8 mM).[21] Perfect continuity of the lattice fringes across the interface between the primary and secondary branches at such an early growth stage implies that the crystal growth is epitaxial rather than an assembly of nanocrystallites.

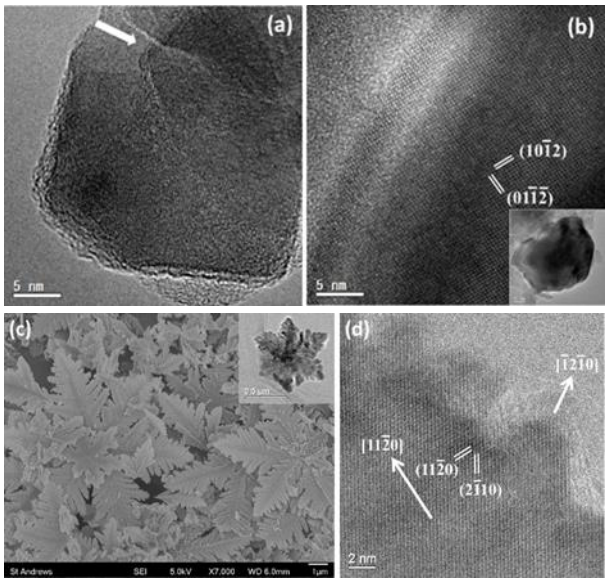

Figure 3. (a,b) HRTEM images of larger nanocrystallites from sample (2 mM, 2 h). The arrow in (a) indicates a thin plate crystal. The inset in (b) shows the corresponding whole crystal with a diameter of about 100 nm. (c) SEM image of snowflake-like hematite crystals in sample (2 mM, 160 min). The inset shows a TEM image of a particle when the 6 primary branches started to appear. (d) HRTEM image of sample (2 mM, 160 min) showing a primary branch surface with evidence of the secondary branches starting to grow. The two arrows indicate growth directions. The marked atomic planes in (b) and (d) are indexed to the hematite structure.

The synthesis with a concentration of 3.8 mM was performed again, and more samples were collected with different reaction times. It was found that the crystal growth followed the same route as discussed above. It includes several key steps: (1) polymerization of the precursor anions, $[Fe(CN)_6]^{3-}$, (2) nucleation inside the disordered aggregates of polymerized ferricyanide anions, (3) crystal growth to about 100 nm in diameter, and finally (4) growth of branches along the <11$\bar{2}$0> directions, forming flat snowflake-shaped hematite crystals. Some SEM images of typical morphologies at different growth stages are shown in Figure S3 in SI.

It has been proposed that the highly selective growth orientations along the <11$\bar{2}$0> zone axes are due to the selective adsorption of $[Fe(CN)_6]^{3-}$ anions on the {11$\bar{2}$0} surfaces of hematite crystals.[21] Ferricyanide has a low dissociation constant therefore these anions are the dominant precursor ions in the solution, while the amounts of Fe^{3+}, O^{2-}, and other Fe-containing ions are negligible. If the crystal surface has some positively charged sites, the interaction between the $[Fe(CN)_6]^{3-}$ anions and such a crystal surface would be enhanced.

In neutral or basic conditions, all the Fe cations on the hematite surface are fully coordinated by six oxygen anions and all the surface oxygen anions are in the form of hydroxyls. The overall charge of these hydroxyl sites depends on how many Fe^{3+} they are coordinated to.[31] As each Fe^{3+} cation is coordinated to six oxygen anions, it contributes 0.5+ charge to each Fe-O bond. Free hydroxyls have a charge of 1−. If the hydroxyl is coordinated to only one Fe^{3+}, the site will be negatively charged (0.5−). The hydroxyls coordinated with two Fe^{3+} give neutral sites. Those coordinated with three Fe^{3+} form positively charged (0.5+) sites.

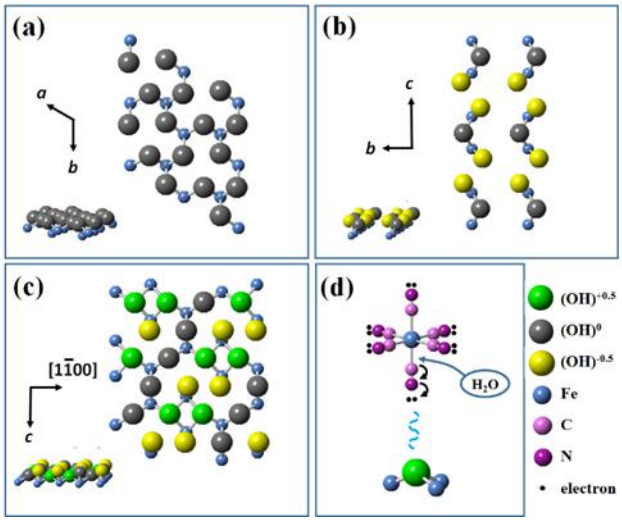

Figure 4. Schematic of the structures of the (a) (0001), (b) (10$\bar{1}$0) and (c) (11$\bar{2}$0) surfaces of hematite in a neutral or basic solution. (d) An illustration of the interaction between a $[Fe(CN)_6]^{3-}$ anion and a positively charged hydroxyl site on the crystal surface.

Figure 4 shows charged sites on three principal surfaces of hematite. On the (0001) surface, all the OH groups are coordinated with two Fe^{3+} (Figure 4a). Therefore, all the OH groups on that surface are neutralized. The (10$\bar{1}$0) surface has hydroxyls which are either singly or doubly coordinated by Fe^{3+} with a ratio of 2 : 1 (5.8/nm^2 and 2.9/nm^2, respectively) and so are overall negatively charged without positively charged sites (Figure 4b). Both the (0001) and (10$\bar{1}$0) surfaces are, therefore, inactive for bonding with the negative ferricyanide anions. The (11$\bar{2}$0) surface, on the other hand, contains all three types of coordinations (5.0/nm^2 for each type of site)[32] (Figure 4c). The positively charged sites on the triply coordinated hydroxyl groups can act as Lewis acidic centres, attracting the $[Fe(CN)_6]^{3-}$ anions. The positive charge on the crystal surface enhances hydrolysis of the $[Fe(CN)_6]^{3-}$ anions by weakening the Fe-C bond as shown in Figure 4d, forming a new deposition layer of Fe_2O_3. Since the driving force of the attraction is a Coulomb force rather than a diffusion process, the growth of branches is fast. Consequently, the {11$\bar{2}$0} surfaces are the most active surfaces of the crystal growth, leading to the formation of snowflake-like crystals.

Feather-like hematite. Upon increasing the precursor concentration to 9 mM or 10 mM, the morphology of the hematite particles significantly changed to feather-like as shown in Figure 1b. Firstly, the primary branches (the main stems) are much longer, over 10 μm, in comparison with the primary branches in the snowflake-like particles. Secondly, the branches are much thinner, with a uniform diameter and their growth directions are even more monotonous. Thirdly and more importantly, the particles are not flat.

Typical feather-like crystals are shown in Figure 5a. The branched particle in the centre of the image shows that the feather-like particles also grew out from a single core. The individual feather-like branches could be fragments broken from larger particles with six branches. Assuming all the secondary branches on the same side of a primary branch are lying in the same plane, the inter-plane angle between the secondary branches on both sides of a primary branch is not 180º, which results in the particles having two different faces. Taking the terms from ancient Chinese philosophical concepts '*yin* and *yang*', we define the face with a smaller angle between the two edges containing secondary branches (the concave face) as '*yin*' and the other side (the convex face) as '*yang*', as marked in the image. The '*yin*' face has a smooth surface on the central stem, while a line of separated nanoparticles can be seen on the central stem of the '*yang*' face.

The primary branch marked '*yang*' upturns from the central particle, while the branch marked '*yin*' downturns (Figure 5a). All of the secondary branches that grow on the upturned primary branches would be downturned, and vice versa. That means the crystal growth directions cannot be along the <11$\bar{2}$0> zone axes, otherwise all the growth directions must lie down on the same plane. The inset of Figure 5a shows a TEM image of the meticulous construction of primary, secondary and tertiary branches, marked by P, S, and T, respectively.

Figure 5b and 5c show a TEM image of another feather-like particle and the corresponding SAED pattern. The latter demonstrates that the whole particle seems to be a single crystal. This property can be regarded as a consequence of the epitaxial growth of branches as shown in Figure 3d. The crystal orientation along the primary branch directly observed from Figure 5b is [10$\bar{1}$2], marked by the arrow A, which is commonly detected from many particles. However, this direction may not be the growth direction, if the primary branch is not perpendicular to the electron beam. When we found a particle with six primary branches and looked down the [0001] zone axis, the observed orientations along the branches were <10$\bar{1}$0>. Generally speaking, the true growth directions should be <10$\bar{1}$*l*> with *l* to be

determined. This problem of projecting a 3D structure into a 2D image was discussed in our previous minireview.[33] The arrows labelled B in Figure 5b show the crystal orientations corresponding to the observed diffraction spots $(01\bar{1}1)$ and $(1\bar{1}01)$. The arrows labelled C show the projected inter-axis angle of the secondary branches on the two sides.

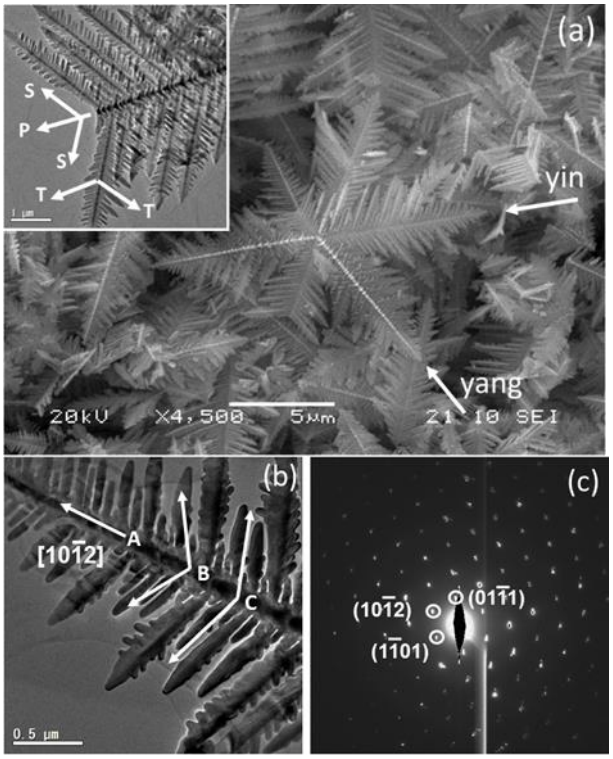

Figure 5. (a) SEM image of sample (10 mM, 48 h), showing feather-like particles. The central particle shows several feather-like branches from a single core. The two faces of the branches are designated '*yin*' and '*yang*'. The inset is an enlarged TEM image. The projected growth directions of the primary (P), secondary (S) and tertiary (T) branches are indicated. (b) TEM image of a broken feather-like particle. The arrow marked A marks the $[10\bar{1}2]$ crystal orientation of the primary branch, B show the crystal orientations corresponding to the observed diffraction spots $(01\bar{1}1)$ and $(1\bar{1}01)$ whilst C marks the projected inter-axis angle of the secondary branches on two sides. (c) The corresponding SAED pattern from the particle in (b).

To determine l in the true growth direction $<10\bar{1}l>$, we applied two methods. First, we found a feather-like particle in TEM and rotated around the short axis of a targeted branch (The short axis is defined to be an axis perpendicular to both the long axis of the branch and the electron beam). The projected length of the branch in question would change. When the projected length was at its maximum value, the branch was perpendicular to the electron beam. At this position, the observed orientation along the branch in HRTEM and SAED was parallel to the growth direction. We found the true growth directions in the feather-like particles were $<10\bar{1}1>$ (see Figure S4 in SI).

In the second method, we measured the inter-axis angle between secondary branches on the two sides of a primary branch in SEM images during rotation around the short axis of the primary branch. When the measured angle was smallest, the plane containing secondary branches on both sides was perpendicular to the beam. Figure S5 in SI shows one set of SEM images for such a test with the smallest angle found to be about 112º. According to the unit cell parameters, a = 5.0356 and c = 13.7489 Å, the inter-axis angles between $[10\bar{1}0]$ and $[\bar{1}100]$ is 120º, between $[10\bar{1}1]$ and $[\bar{1}101]$ is 111.28º, while the angle between $[10\bar{1}2]$ and $[\bar{1}102]$ is 93.99º and between $[10\bar{1}3]$ and $[\bar{1}103]$ is 77.72º. Consequently, the highly selective growth direction along $<10\bar{1}1>$ in the feather-like hematite crystals can be confirmed.

In the rhombohedral structure of hematite, a 3-fold symmetry is applied to the $\{10\bar{1}l\}$ planes and 6-fold symmetry to the $\{11\bar{2}l\}$ planes. Unlike the snowflake-like particles with branch growth along 6 identical $<11\bar{2}0>$ directions, the branch growth in feather-like crystals is along 3 $<10\bar{1}1>$ directions upward and another three directions downward.[34] This agrees what we observed in Figure 5a.

Leaf-like hematite. When the concentration of the precursor was increased to a range from 100 mM to 500 mM, the morphology of the hematite crystals was no longer feather-like. Figure 6a shows some typical particles from this sample. Although the tertiary branches are still fine with almost a uniform diameter in each branch, the secondary branches extend on both sides. The morphology is like fern leaves as can be observed from the low magnification image showing an overview of the morphology in Figure 6b.

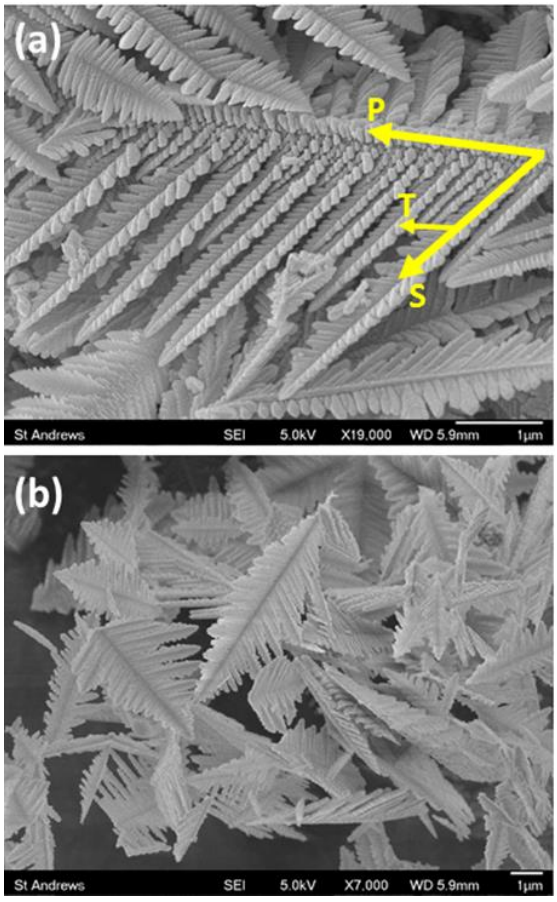

Figure 6. SEM images of hematite crystals with a leaf-like morphology. (a) Image at a larger magnification from sample (100 mM, 90 min). The primary, secondary and tertiary branches are indicated by P, S, and T, respectively. (b) Image at a low magnification for an overview from sample (500 mM, 3 h).

When the concentration of ferricyanide was further increased to 500 mM, both the secondary and tertiary branches became wider and the morphology of the crystals produced was more leaf-like (Figure 1c, Figure S6 in SI). Using the same methods as described above for the feather-like crystals, it has been confirmed that the growth orientations of leaf-like crystals are also along the <10$\bar{1}$1> zone axes.

To investigate the growth mechanism of these feather-like and leaf-like crystals, many specimens using 500 mM of ferricyanide were collected over a range of growth times (see Table S1 in SI) and their morphologies and microstructures were examined.

At an early stage, the precipitate was also amorphous as shown by SEM in Figure S7 in SI. TEM images of these aggregates at a high concentration of ferricyanide show that they are much larger and denser than the aggregates formed in low concentration conditions (see Figure S8 in SI). Although a drying effect of the specimen suspension on the sample grid may lead to further aggregation, using dilute suspensions to make the above comparison is often effective. In addition, some fibre-like particles can be seen inside the aggregates (see Figure S8d in SI), which could be a consequence of polymerization of a large amount of ferricyanide.

Nucleation and crystal growth took place near the surfaces of the polymer aggregates (see Figure S9 in SI). Figure 7 shows HRTEM images of small crystallites found in sample (500 mM, 30 min).

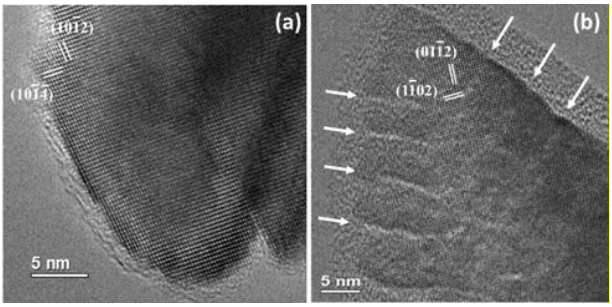

Figure 7. (a) HRTEM image of a typical crystal without branches from sample (500 mM, 30 min). (b) HRTEM image of a tip of a crystallite from the same sample, in which branches have just started to grow. The gaps between the branches are indicated by the arrows.

The crystallite in Figure 7a gives a different image contrast in the centre, indicating that the centre has a lower crystallinity. Such a structure is unlikely developed from single nucleation. A possible formation mechanism of this structure is extension and merger of surface crystallites, leading to a single crystalline surface.

The message conveyed by the HRTEM image in Figure 7b is of interest. When the primary branches grow out from the central particle, their diameter is restricted by the size of that particle. If a primary branch grows to a certain length before any secondary branches start to appear, the growth of the secondary branches on the sides of the primary branch, even specific to the <10$\bar{1}$1> zone axes, would lead to two plates rather than the separated rod-shaped branches. A typical example is the formation of triple-wing C_{60}/trimethylbenzene nanowires.[18] The image in Figure 7b implies that the growth of the secondary branches must occur almost simultaneously with the growth of the primary branch.

Surface acidity driven crystal growth directions. It is extraordinary that the crystal growth direction of hematite is so highly selective during hydrolysis without the need for the addition of any chemical additives. It is even more surprising to see that the growth direction can change from <11$\bar{2}$0> to <10$\bar{1}$1> simply by increasing the concentration of ferricyanide, leading to a morphology change from snowflake-like to feather-like and leaf-like. If the proposed mechanism relying on the charge of surface hydroxyl groups is correct, the effect of the ferricyanide concentration on the surface property must be by way of changing the pH value of the solution. It is widely known that the presence of hydroxyl groups on the surface is pH dependent.

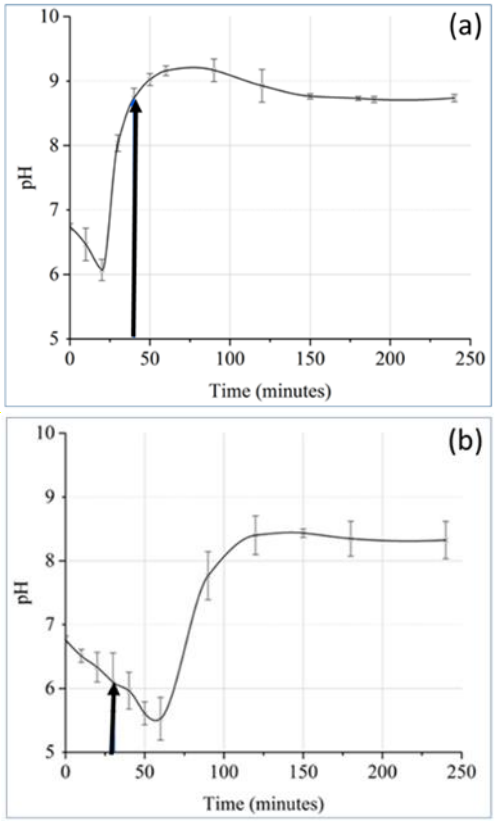

Figure 8. Change of solution pH values during hydrolysis of ferricyanide as a function of reaction time. Different concentrations of ferricyanide are plotted where (a) is 3.8 mM and (b) is 500 mM. The arrows indicate the points at which the branches of hematite start to grow. The error bars are the standard deviations of three data points.

Two concentrations of ferricyanide were selected to examine pH changes with the reaction time, from which hematite crystals were produced. One is low concentration, 3.8 mM, and another is high concentration, 500 mM, giving rise to snowflake-like and leaf-like crystals, respectively. pH values of the synthetic solutions were recorded at different stages and the results are shown in Figure 8. In both cases, the pH value initially drops down and then starts to increase at a certain point. This result supports our observation of polymerization as the first step of partial hydrolysis of ferricyanide anions, since this chemical

process would release HCN as seen in equations (2) and (3) above. HCN is a weak acid with an acid dissociation constant, K_a associated to equation (4), of 6.2×10^{-10}. Increasing HCN concentration would reduce the pH value.

When the ferricyanide anions are fully hydrolyzed to form hematite crystals, the overall reaction is

$$2[Fe(CN)_6]^{3-} + 3H_2O \rightarrow Fe_2O_3 + 6HCN + 6CN^- \quad (5)$$

followed by

$$CN^- + H_2O \xrightarrow{Kb} HCN + OH^- \quad (6)$$

The reaction (5) releases HCN and CN^- in a 1 : 1 ratio. According to the much higher base dissociation constant, K_b for equation (6), of 2.0×10^{-5}, the pH of the solution will increase. The turning point in the 3.8 mM solution is at pH $\approx$ 6 at a time of about 20 min, while in the 500 mM solution, the turning point is at pH $\approx$ 5.4 at a time of about 55 min. This means the polymerization of ferricyanide anions in the high concentration solution dominates for a longer time and so the corresponding total amount of HCN released is larger. Obviously, the turning point is a balanced position between polymerization with a reduction of pH and crystallization with an increase of pH. The starting points of nucleation and primary crystal growth must be earlier than these turning points.

The rate of nucleation and growth of the core crystals in the high concentration solution is relatively slower. This is because the polymer particles in the high concentration system are larger and denser (see Figure S8 in SI), leading to a relatively smaller specific surface area and less chance for water to diffuse into the inner areas of the particles. There are, therefore, a smaller proportion of active sites for nucleation and incipient crystal growth (see Figure S9 in SI). Full hydrolysis of ferricyanide to hematite crystals takes a longer time. The increase of pH value in the high concentration system is slower as shown in Figure 8.

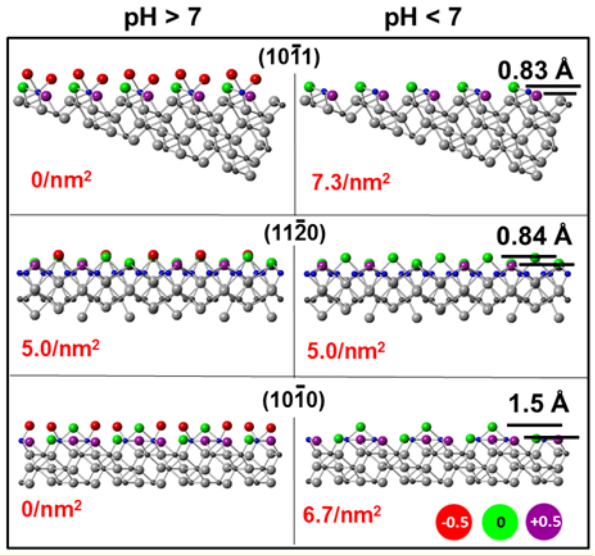

Figure 9. Schematic of three principal surface structures of hematite crystals in basic conditions where all the hydroxyls are maintained, and in acidic conditions where all the singly coordinated hydroxyl groups are removed. The density of positively charged hydroxyl sites (purple) coordinated with three Fe and the depth of their location from the top atomic layer are indicated.

It was observed that, in the 3.8 mM system, short branches did not appear until after 40 min. At this point, the pH was about 8.5 (Figure 8a). In the 500 mM solution, the branches started to grow after a reaction time of 30 min, when the pH was about 6 and was still decreasing (Figure 8b). SEM images from both samples with short branches just appearing are shown in Figure S10 in SI. The basic conditions at low concentrations of ferricyanide would protect the surface hydroxyl groups and so the charged sites shown in Figure 4 can be maintained. However, under acidic conditions in the high concentration solution, some surface hydroxyl groups may be unstable and removed. We assume all the hydroxyl groups coordinated with only one iron cation are removed, and so the distribution of the charged sites on crystal surfaces must be changed (Figure 9).

The {0001} surface contains only two coordinated hydroxyl groups and the pH value has no effect on its electronic structure (Figure 4a). When the concentration of ferricyanide changes from basic to acidic conditions, the density of 0.5+ charged hydroxyl sites on the {10$\bar{1}$0} surfaces changes from 0/nm^2 to 6.7/nm^2. No such density change takes place on the {11$\bar{2}$0} surfaces, where the number of the 0.5+ charged hydroxyls remains 5.0/nm^2. The positively charged hydroxyl sites on the {10$\bar{1}$1} surfaces increases from 0/nm^2 to 7.3/nm^2 (Figure 9). The depth of these three coordinated hydroxyls from the top surface atomic layer on the {10$\bar{1}$0}, {11$\bar{2}$0} and {10$\bar{1}$1} surfaces are 1.5, 0.84 and 0.83 Å, respectively, as indicated in Figure 9. A top view of these surfaces is presented in Figure S11 in SI.

Additionally, removing singly coordinated hydroxyls will cause some Fe cations to be exposed at the surface, giving extra positively charged sites. The charge density associated with these sites on the {10$\bar{1}$0}, {11$\bar{2}$0} and {10$\bar{1}$1} surfaces are 3.3+, 4.6+ and 7.3+ per nm^2 respectively. The depth of these sites are 1.37, 1.77 and 0.50 Å. The overall charge density on these three principal surfaces are 6.6+, 7.1+ and 10.9+ per nm^2 (Table S2 in SI). Consequently, the {10$\bar{1}$1} surfaces give a higher density of positive charge and a smaller depth of these charged sites. The crystal growth orientation, therefore, changes to <10$\bar{1}$1>.

There is another interesting consequence induced by removing all the singly coordinated hydroxyls under acidic conditions. All Fe cations on the {10$\bar{1}$1} surfaces link to 2 singly coordinated hydroxyls under basic conditions. When these hydroxyls are removed in acidic conditions, the Fe cations would remain with a charge of 1+ rather than 0.5+ on other surfaces. The strong local charge would further increase the power of attracting ferricyanide anions.

The principal growth orientations of the feather-like and leaf-like crystals are the same. The main difference is that, when the concentration of ferricyanide is relatively low, *e.g.* 9 mM or 10 mM, the crystal growth direction is highly selective and restricted to the <10$\bar{1}$1> zone axes. The diameter of each branch is, therefore, uniform. At a high concentration of the precursor, *e.g.* 500 mM, the crystal growth orientation is relatively less selective. In other words, growth along other directions also occurs. The shape of the branches becomes thicker, looking more like leaves. Increasing the reaction time with a high ferricyanide concentration tends to lead to the formation of leaf-like crystals because the pH value would increase with the reaction time.

In summary, Figure 10 shows an illustration of the crystal growth of hematite during the hydrolysis of $[Fe(CN)_6]^{3-}$. At the very beginning, ferricyanide anions are not hydrolyzed into individual iron hydroxide molecules, but form dimers, trimers (Figure 10a) followed by forming large polymer particles (Figure 10b). Nucleation and early stage crystal growth occur near

the surface of the polymer particles (Figure 10c). The crystallites grow up to about 100 nm in diameter without any branches (Figure 10d). Fast growth of branches then takes place along highly selective crystal orientations depending on the pH value of the solution. When the concentration of ferricyanide is low, the pH value at the point of branch growth is larger than 7 and the growth is along the six equivalent <11$\bar{2}$0> directions (Figure 10e). This results in flat snowflake-like particles (Figure 10f). When the concentration of ferricyanide is high, the pH value at the point of branch growth is smaller than 7, the growth directions are along six <10$\bar{1}$1> zone axes (Figure 10g), leading to non-flat feather-like (Figure 10h) or leaf-like (Figure 10i) morphologies.

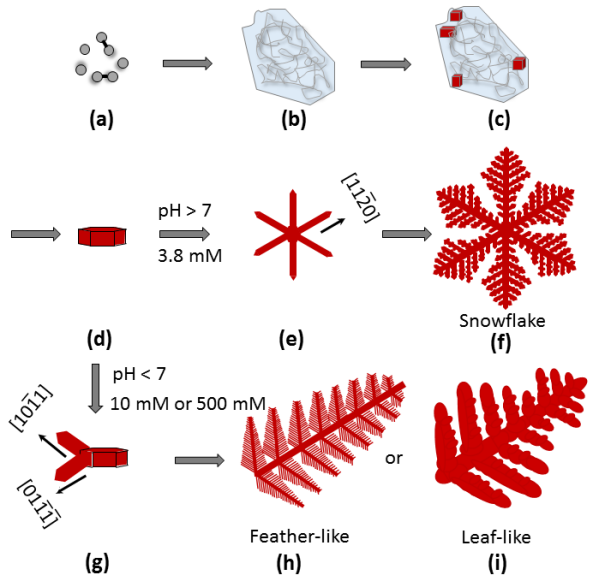

Figure 10. Schematic showing crystal growth of hematite during hydrolysis of ferricyanide and the morphology change as a function of the concentration of ferricyanide.

CONCLUSIONS

This work demonstrates that crystal growth may not follow the classical theory even in a simple system, such as an aqueous solution of $K_3Fe(CN)_6$ for growing hematite crystals via hydrolysis of $[Fe(CN)_6]^{3-}$ where no additional additives are involved. The polymerization of the ferricyanide anions disturbs the environment for the nucleation of free crystals and instead shifts the nucleation sites from the solution to the surfaces of the polymer particles. The crystal growth rate is not only governed by the internal factors of the crystal, including surface binding energy, but is also dependent on the properties of the precursor, and the interactions between the precursor ions and the crystal surface.

The precursor pieces and building units for crystal growth in a synthetic solution are often different. In the present work, the concentrations of building units, Fe^{3+} and O^{2-}, are very low. The active precursor moving to the crystal surface and contributing to the crystal growth is $[Fe(CN)_6]^{3-}$, which has a significantly different charge from Fe^{3+}. Hence, the density of Lewis acidic sites on the crystal surfaces plays an important role in the highly selective growth directions. Our recent work also demonstrates a similar mechanism of surface charge driven growth of eight-branched Cu_2O crystals.[35] Establishing this mechanism allows us to understand the variation of pH value during the hydrolysis of ferricyanide and the corresponding change of crystal growth orientation from {11$\bar{2}$0} (pH >7) to {10$\bar{1}$1} (pH <7). This mechanism is complementary to the classical crystal growth theory and may enable us to control growth directions for many other crystals.

SUPPORTING INFORMATION

Synthetic conditions, XRD patterns, EDX spectra, more SEM and TEM images and crystal surface structures are supplied as Supporting Information. This material is available free of charge via the Internet at http://pubs.acs.org.

AUTHOR INFORMATION

Corresponding Author
E-mail: wzhou@st-andrews.ac.uk

ACKNOWLEDGEMENTS

We thank Benjamin Walden and Johnathan Marshall for their contribution to synthesis of some samples during their miniproject. W.Z. thanks EPSRC for financial support to purchase the FEG SEM (EP/F019580/1).

REFERENCES

(1) Burda, C.; Chen, X.; Narayanan, R.; El-Sayed, M. A. Chemistry and Properties of Nanocrystals of Different Shapes. *Chem. Rev*. **2005**, *105*, 1025–1102.

(2) Bravais, A. *Études Cristallographiques*. Gauthier-Villars, Paris, **1866**.

(3) Friedel, M. G. Études sur la loi de Bravais. *Bull. Soc. Fr. Mineral Cristallogr*. **1907**, *30*, 326–455.

(4) Donnay, J. D. H.; Harker, D. A New Law of Crystal Morphology Extending the Law of Bravais. *Am. Mineral*. **1937**, *22*, 446–467.

(5) Curie, P. On the Formation of Crystals and on the Capillary Constants of Their Different Faces. *Bull. Soc. Fr. Mineral Cristallogr*. **1885**, *8*, 145–150.

(6) Wulff, G. On the Question of Speed of Growth and Dissolution of Crystal Surfaces. *Z. Kristallogr*. **1901**, *34*, 449–530.

(7) Chen, X. Y.; Qiao, M. H.; Xie, S. H.; Fan, K. N.; Zhou, W. Z.; He, H. Y. Self-Construction of Core-Shell and Hollow Zeolite Analcime Icositetrahedra: A Reversed Crystal Growth Process via Oriented Aggregation of Nanocrystallites and Recrystallization from Surface to Core. *J. Am. Chem. Soc*. **2007**, *129*, 13305–13312.

(8) Yao, J. F.; Li, D.; Zhang, X. Y.; Kong, C. H.; Yue, W. B.; Zhou, W. Z.; Wang, H. T. Cubes of Zeolite A with an Amorphous Core. *Angew. Chem. Int. Ed*. **2008**, *47*, 8397–8399.

(9) Self, K.; Zhou, H. J.; Greer, H. F.; Tian, Z. R.; Zhou, W. Z. Reversed Crystal Growth of ZnO Microdisks. *Chem. Commun*. **2013**, *49*, 5411–5413.

(10) Yu, F. J.; Zhou, W. Z. Alloying and Dealloying of CuPt Bimetallic Nanocrystals. *Prog. Nat. Sci. Mater. Int*. **2013**, *23*, 331–337.

(11) Ross, F. M. Controlling Nanowire Structures Through Real Time Growth Studies. *Rep. Prog. Phys*. **2010**, *73*, 114501.

(12) Su, Z. X.; Dickinson, C.; Wan, Y. T.; Wang, Z. L.; Wang, Y. W.; Sha, J.; Zhou, W. Z. Crystal Growth of Si Nanowires and Formation of Longitudinal Planar Defects. *CrystEngComm* **2010**, *12*, 2793–2798.

(13) Zhu, K. K.; He, H. Y.; Xie, S. H.; Zhang, X.; Zhou, W. Z.; Jin, S.; Yue, B. Crystalline WO_3 Nanowires Synthesized by Templating Method. *Chem. Phys. Lett*. **2003**, *377*, 317–321.

(14) Zhu, K. K.; Yue, B.; Zhou, W. Z.; He, H. Y. Preparation of Three-dimensional Chromium Oxide Porous Single Crystals Templated by SBA–15. *Chem. Commun*. **2003**, 98–99.

(15) Polleux, J.; Pinna, N.; Antonietti, M.; Niederberger, M. Ligand-Directed Assembly of Preformed Titania Nanocrystals into Highly Anisotropic Nanostructures. *Adv. Mater*. **2004**, *16*, 436–439.

(16) Yu, F. J.; Xu, X. X.; Baddeley, C. J.; Bellabarba, R. M.; Lignier, P.; Tooze, R. P.; Fina, F.; Irvine, J. T. S.; Zhou, W. Z. Surface Ligand

Mediated Growth of CuPt Nanorods. *CrystEngComm* **2014**, *16*, 1714–1723.

(17) Wang, X.; Ozkan, C. S. Multisegment Nanowire Sensors for the Detection of DNA Molecules. *Nano Lett*. **2008**, *8*, 398–404.

(18) Geng, J. F.; Zhou, W. Z.; Skelton, P.; Yue, W. B.; Kinloch, I. A.; Windle, A. H.; Johnson, B. F. G. Crystal Structure and Growth Mechanism of Unusually Long Fullerene (C_{60}) Nanowires. *J. Am. Chem. Soc*. **2008**, *130*, 2527–2534.

(19) Zhou, Y. N.; Zhou, W. Z. Growth Mechanism of C_{60}/mesitylene Manowires. *CrystEngComm* **2012**, *14*, 1449–1454.

(20) Cao, M. H.; Liu, T. F.; Gao, S.; Sun, G. B.; Wu, X. L.; Hu, C. W.; Wang, Z. L. Single-Crystal Dendritic Micro-Pines of Magnetic α-Fe_2O_3: Large-Scale Synthesis, Formation Mechanism, and Properties. *Angew. Chem. Int. Ed*. **2005**, *44*, 4197–4201.

(21) Liu, Z.; Chiang, C.-Y.; Li, W.; Zhou, W. Z. The Role of Surface Hydrolysis of Ferricyanide Anions in Crystal Growth of Snowflake-shaped α-Fe_2O_3. *Chem. Commun*. **2015**, *51*, 9350–9353.

(22) Chirita, M.; Grozescu, I. Fe_2O_3–Nanoparticles, Physical Properties and Their Photochemical and Photoelectrochemical Applications. *Chem. Bull. POLITEHNICA Univ. (Timişoara)* **2009**, *54*, 1–8.

(23) Polshettiwar, V.; Baruwati, B.; Varma, R. S. Self-Assembly of Metal Oxides into Three-Dimensional Nanostructures: Synthesis and Application in Catalysis. *ACS Nano* **2009**, *3*, 728–736.

(24) Jiao, Y.; Liu, Y.; Qu, F.; Wu, X. Dendritic α-Fe_2O_3 Hierarchical Architectures for Visible Light Driven Photocatalysts. *CrystEngComm* **2014**, *16*, 575–580.

(25) Hu, X.; Yu, J. C.; Gong, J. Fast Production of Self-Assembled Hierarchical α-Fe_2O_3 Nanoarchitectures. *J. Phys. Chem. C* **2007**, *111*, 11180–11185.

(26) Xia, Y.; Yang, P.; Sun, Y.; Wu, Y.; Mayers, B.; Gates, B.; Yin, Y.; Kim, F.; Yan, H. One-Dimensional Nanostructures: Synthesis, Characterization, and Applications. *Adv. Mater*. **2003**, *15*, 353–389.

(27) Bharathi, S.; Nataraj, D.; Seetha, M.; Mangalaraj, D.; Ponpandian, N.; Masuda, Y.; Senthil, K.; Yong, K. Controlled Growth of Single-crystalline, Nanostructured Dendrites and Snowflakes of α-Fe_2O_3: Influence of the Surfactant on the Morphology and Investigation of Morphology Dependent Magnetic Properties. *CrystEngComm* **2010**, *12*, 373–382.

(28) Jiang, Z.; Jiang, D.; Wei, W.; Yan, Z.; Xie, J. Natural Carbon Nanodots Assisted Development of Size-tunable Metal (Pd, Ag) Nanoparticles Grafted on Bionic Dendritic α-Fe_2O_3 for Cooperative Catalytic Applications. *J. Mater. Chem. A* **2015**, *3*, 23607–23620.

(29) Wang, X.; Wang, J.; Cui, Z.; Wang, S.; Cao, M. Facet Effect of α-Fe_2O_3 Crystals on Photocatalytic Performance in the Photo-Fenton Reaction. *RSC Adv*. **2014**, *4*, 34387–34394.

(30) Liu, Z.; Lv, B. L.; Wu, D.; Zhu, Y.; Sun, Y. H. Precisely Tailoring Dendritic α-Fe_2O_3 Structures Along $[10\bar{1}0]$ directions. *CrystEngComm* **2012**, *14*, 4074–4080.

(31) Barrón, V.; Torrent, J. Surface Hydroxyl Configuration of Various Crystal Faces of Hematite and Goethite. *J. Colloid Interface Sci*. **1996**, *177*, 407–410.

(32) Rochester, C. H.; Topham, S. A. Infrared Study of Surface Hydroxyl Groups on Haematite. *J. Chem. Soc., Faraday Trans. 1* **1979**, *75*, 1073–1088.

(33) Zhou, W. Z.; Greer, H. F. What Can Electron Microscopy Tell Us Beyond Crystal Structures? *Eur. J. Inorg. Chem*. **2016**, 941–950.

(34) Lin, M.; Tng, L.; Lim, T.; Choo, M.; Zhang, J.; Tan, H. R.; Bai, S. Hydrothermal Synthesis of Octadecahedral Hematite (α-Fe_2O_3) Nanoparticles: An Epitaxial Growth from Goethite (α-FeOOH). *J. Phys. Chem. C* **2014**, *118*, 10903–10910.

(35) Self, K.; Zhou, W. Z. Surface Charge Driven Growth of Eight-branched Cu_2O Crystals. *Cryst. Growth Des*. **2016**, *16*, 5377–5384.

For Table of Contents Use Only (TOC)

Growth Mechanism of Dendritic Hematite via Hydrolysis of Ferricyanide

Alice E. Green, Chang-Yang Chiang, Heather F. Greer, Ashleigh Waller, Aron Ruszin, James Webster, Ziyin Niu, Katherine Self and Wuzong Zhou

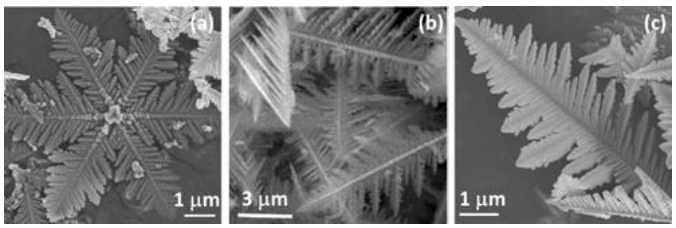

Synopsis: Highly selective growth directions of hematite crystals during hydrolysis of ferricyanide has been found to be driven by charge on the crystal surface, based on which a new growth mechanism being established.